applied sciences

MDPI

Article

Multi-Timescale Control of Variable-Speed Wind Turbine for Inertia Provision

Zixiao Xu [1], Yang Qi [1], Weilin Li [1] and Yongheng Yang [2,*]

[1] School of Automation, Northwestern Polytechnical University, Xi'an 710072, China; xuzixiao_9602@mail.nwpu.edu.cn (Z.X.); qiyang@nwpu.edu.cn (Y.Q.); liweilin907@126.com (W.L.)
[2] College of Electrical Engineering, Zhejiang University, Zheda Rd 38, Hangzhou 310027, China
* Correspondence: yang_yh@zju.edu.cn

Abstract: The increasing deployment of power converters has led to a significant reduction in the power system inertia and consequently resulted in frequency stability issues. To improve the robustness of the grid against frequency disturbances, it is becoming more expected in many countries that renewable energy generation, such as wind turbine power systems, should provide equivalent inertia support to the power system. This can be achieved through advanced control of power converters, in addition to adding extra energy storage devices, e.g., batteries. In wind turbine systems, although the ancillary service of inertia provision can be realized by coupling the rotor speed with the grid frequency, the rotor speed recovery process affects the inertia response if the controller is not properly designed or well-tuned. To address this issue, in this paper, we propose a multi-timescale control strategy for a doubly fed induction generator (DFIG) wind turbine system. Synthetic inertia control and speed recovery control are simultaneously incorporated into the controller of the rotor-side converter, whereas their dynamics are decoupled under different timescales to avoid control conflict. Extensive simulation results are provided, which validate the efficacy of the proposed inertia emulation scheme.

Keywords: wind turbine; inertia emulation; power converter; frequency stability; primary frequency response

Citation: Xu, Z.; Qi, Y.; Li, W.; Yang, Y. Multi-Timescale Control of Variable-Speed Wind Turbine for Inertia Provision. *Appl. Sci.* **2022**, *12*, 3263. https://doi.org/10.3390/app12073263

Academic Editor: Mohsen Soltani

Received: 12 February 2022
Accepted: 22 March 2022
Published: 23 March 2022

1. Introduction

The increasing penetration of renewable energy resources (RESs), such as the photovoltaic (PV) panels and wind turbines, has fundamentally changed power system characteristics. These RESs are usually integrated into the power grid through power-electronic converters, which, naturally, do not possess the attribute of mechanical inertia. Conventional synchronous generators (SG) are gradually being replaced by inertia-less power converters (low-inertia systems), which will result in a reduction in power system inertia to a large extent [1–10]. The decrease in the power system inertia, on one hand, will result in a higher rate of change of frequency (RoCoF). On the other hand, the reduction in the power system inertia can cause a low-frequency nadir [2]. As a consequence, frequency stability issues are more likely to happen [3,4]. One recently reported incident is the 2016 Australia blackout, which affected millions of people and caused considerable economic loss. It is believed that a lack of power system inertia is one of the reasons behind the blackout [5]. Therefore, it is of importance in many countries to increase power system inertia and enhance the frequency stability of future power-electronics-dominated power system, where more and more renewable energy resources are adopted.

To achieve this objective, a number of research activities have explored the possibility of using power-electronics converters to provide grid inertia support [6–8], in addition to the use of extra energy resources, e.g., batteries. Among them, the virtual synchronous generator (VSG) technique stands out as a promising solution. The VSG control strategy enables the power converter to emulate the rotor swing equation of a conventional SG.

As a consequence, the dynamic of the converter is similar to that of the SG. Nevertheless, the successful implementation of the VSG control strategy usually requires a bulky and costly energy storage system to provide active power support. Alternatively, the electrical energy stored in DC-link capacitors can also be utilized to provide inertia support [10]. To achieve this objective, large DC capacitors are normally required, which may not conform with the power-electronics converter design principle. In [11,12], the voltage across a supercapacitor was proportionally linked with the AC power grid. Through this effort, the supercapacitor can be controlled to behave similarly to a virtual synchronous generator to support the power system frequency response. Alternatively, the inertia emulation effect can be equivalently achieved by demand-side management techniques. In [13], the power consumptions of certain noncritical loads, such as electric heating, lighting, and cooling, were adaptively regulated to realize synthetic inertia and suppress the power grid RoCoF and frequency deviation.

The inertia emulation target can also be achieved by PV generation systems. Conventionally, the PV inverter operates under maximum power point tracking (MPPT) mode, which harvests the maximum solar energy and does not participate in grid frequency regulation [14]. Recently, power reserve control (PRC) and active power curtailment control were developed to intentionally reduce the PV output power and spare a certain amount of active power for inertia provision [15–18]. Through this effort, the requirement of energy storage units, capacitors, and supercapacitors becomes unnecessary and largely alleviated. Accordingly, an event-triggering control strategy was developed to switch the PV system between different operation modes to optimize the frequency support from the reserved power [19]. A coordination scheme was further proposed to achieve the virtual inertia and frequency-damping effect in [20]. These advanced control algorithms have made PV generation systems more grid-friendly and actively contribute to power system frequency regulation.

In comparison with PV generation systems, wind turbines have even greater potential to provide inertia support. This is because the significant mechanical energy stored in the rotor can be temporarily released to respond to a power grid frequency event. The earlier application can be traced back to the wind turbine system in the Hydro-Quebec system, as well as that in Ontario [21]. For the normal stage, the wind turbine operates at the maximum power point (MPP). When a grid-frequency drop is detected, the reference power of the wind turbine is increased by 5–10% to provide active power support. After a certain amount of time, the wind turbine decreases its output power reference by 30% until the rotor speed is gradually recovered. Similar techniques have also been reported in recent publications. In [22], a supplementary electromagnetic torque component proportionally linked with the grid RoCoF was included to achieve the desired inertia emulation. In [23,24], a high-pass filter was implemented to avoid the high-frequency noise amplification concern. In [25], the dynamics between a type 3 wind turbine and the SG were compared. On this basis, the phase motion of the SG was reconstructed in a wind turbine system to enable the inertia function. In [26], frequency droop control was implemented as an alternative for a synthetic inertia strategy through control parameter optimization. Moreover, in [27], a cascaded control structure was proposed to regulate DC-link energy and subsequently control the rotor kinetic energy to support the grid frequency, which minimizes the impacts on wind energy harvesting. In addition to this, the inertia provision function of a doubly fed induction generator (DFIG) unit was enabled by rotor current control and optimized through status assessment in [28]. In [29], a power management strategy was developed that blends the energy stored in the high-voltage direct current (HVDC) link and the energy of a wind turbine to provide quick frequency responses. Consequently, the power capability requirement of wind turbines can be relieved.

The common principle behind these proposals is to link the power grid frequency (or the RoCoF) with the rotor speed (or the electromagnetic torque) of the wind turbine. It should be mentioned that the wind turbine needs to recover after the settling of a frequency event (i.e., post-event operation). However, the speed recovery process can

significantly affect the inertia-provision effect if it is not properly designed [30]. It is likely that a subsequent frequency drop, as the second frequency event, will occur due to the interaction between speed recovery control and inertia control [2]. For the worst scenarios, the coupling between inertia provision and the dynamic characteristic of a wind turbine system may even affect the small-signal stability of the entire power system and lead to power oscillations [31,32].

To address this problem, a multi-timescale control scheme for inertia provision of a DFIG wind conversion system is proposed in this paper. A schematic diagram of the DFIG power conversion system is shown in Figure 1. By properly selecting the rotor-side converter (RSC) control parameters, the dynamics of inertia control and those of speed recovery control can be decoupled in the frequency domain to avoid control conflict. As a benefit, inertia provision, as well as speed recovery objectives, can be simultaneously achieved.

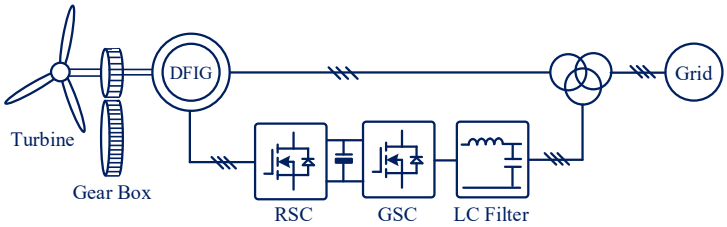

Figure 1. Schematic diagram of the DFIG power conversion system.

Compared to prior-art approaches, the contributions of this paper are summarized as:

(1). Revealing the coupling effect between virtual inertia control and speed recovery control of the wind energy conversion system with an investigation of the corresponding impact on the performance of RoCoF suppression;
(2). Decoupling of rotor speed recovery control and inertia control into different timescales; as a result, the inertia provision and speedy post-event recovery objectives can be simultaneously achieved;
(3). Designing a noise-free approach to acquire the real-time grid RoCoF, the response time of which is less than 0.1 s;
(4). Conducting simulations to verify the theoretical analysis and control performance. With the wind turbine virtual inertia being 5 s, the maximum RoCoF is successfully reduced by around 23%.

The rest of this paper is organized as follows. Section 2 introduces the basic inertia emulation principle. Section 3 discusses the DFIG control strategy, including RSC control, grid-side converter (GSC) control, and acquisition of the power grid RoCoF. Extensive simulation results are provided in Section 4 to verify the theoretical findings and the proposed control scheme. Finally, Section 5 concludes the paper.

2. Principle of Inertia Emulation

2.1. Power System Frequency Response

Figure 2 shows the power system primary frequency regulation framework. For the convenience of a statement, all the variables are displayed in per-unit values. R is the frequency droop coefficient; T_G refers to the speed governor time constant; F_{HP}, T_{RH}, and T_{CH} are the reheat turbine time constants; $\Delta P_{\mathrm{ref\_pu}}$ is the input-power reference variation; $\Delta P_{\mathrm{m\_pu}}$ is the mechanical power variation; and $\Delta P_{\mathrm{l\_pu}}$ is the load power variation. According to the well-known swing equation [8], the power grid frequency, $\Delta f_{\mathrm{g\_pu}}$, is given by:

$$\frac{d}{dt}\Delta f_{\mathrm{g\_pu}} = \frac{1}{2H_M}\left(\Delta P_{\mathrm{m\_pu}} - \Delta P_{\mathrm{l\_pu}}\right) \quad (1)$$

where H_M is the inertia constant of the synchronous machine (SM). Equation (1) indicates that the power grid frequency deviates from the nominal value if there is a power imbalance between the power generation and the load demand. More specifically, Figure 3 illustrates

the typical frequency response when the power grid is subjected to a disturbance (taking a sudden load change as an example).

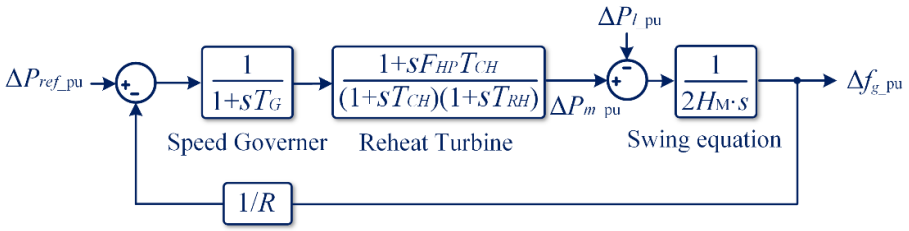

Figure 2. Primary power system frequency regulation framework.

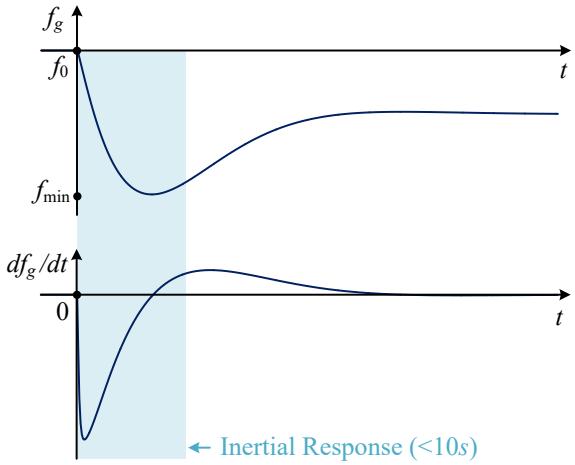

Figure 3. Typical power system frequency response after a disturbance (e.g., a load step change).

Due to the inertia of the SM, the power grid frequency does not immediately drop or increase with a high ramp rate. The instantaneous power imbalance is compensated by the mechanical energy of the rotor, resulting in a comparatively small variation in the system frequency. This process is known as the inertia response and usually takes less than 10 s. For a longer timescale, the speed governor control takes effect, and the frequency finally reaches a new equilibrium point. There are two important metrics that require attention, from the power system frequency stability perspective. One is the frequency nadir ($f_{\min}$ in Figure 3), and the other is the RoCoF value. When the frequency nadir goes beyond the normal operating range, proper measures, such as load shedding, should be taken, which causes a negative impact on electricity customers. In addition to this, the high RoCoF value may also cause a pole slip, trip the SM, and even lead to frequency instability. In this regard, many countries have set stringent requirements for the frequency nadir and the RoCoF.

To illustrate the impact of inertia on the frequency nadir and the RoCoF, Figure 4 shows the grid frequency response with different inertia values. It can be observed that the increase in the power system inertia reduces the RoCoF value and also improves the frequency nadir. Consequently, the power system frequency stability is enhanced. However, when conventional SMs and SGs are gradually replaced by inertia-less power converters, the total inertia of the power grid will decrease, giving ride to frequency stability concerns. Therefore, it is of importance to enable power converters to make an active contribution to the power grid by properly providing grid support, e.g., emulating inertia.

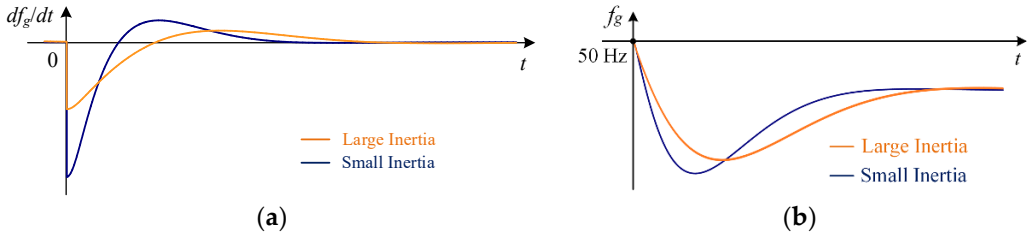

(**a**) (**b**)

Figure 4. Grid frequency response with different inertia values. (**a**) Comparison of RoCoF. (**b**) Comparison of grid frequency.

2.2. Inertia Provision Principle

To achieve this objective, the output power of renewable energy resources (RESs) needs to be coupled with the power grid frequency. Figure 5 illustrates the inertia provision principle, where H_v is the virtual inertia provided by RESs, and $\Delta P_{\text{i\_pu}}$ is the output power variation of the RES.

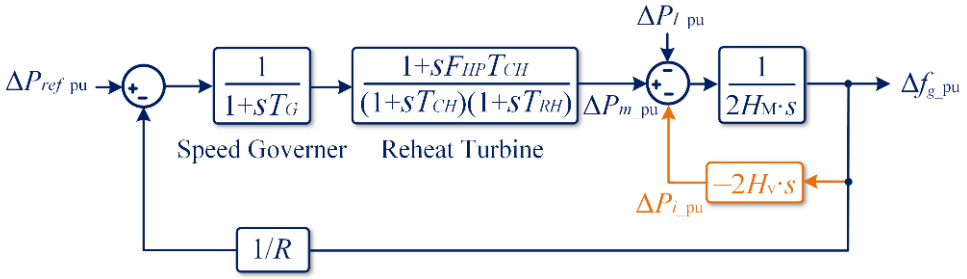

Figure 5. General control block diagram for inertia provision from RES systems.

From Figure 5, it can be seen that the power system frequency variation, $\Delta f_{\text{g\_pu}}$, is given by:

$$\frac{d}{dt}\Delta f_{\text{g\_pu}} = \frac{1}{2H_M}\left(\Delta P_{\text{m\_pu}} - \Delta P_{\text{l\_pu}} - \Delta P_{\text{i\_pu}}\right) \tag{2}$$

given that the RES active power variation is proportionally linked to the grid RoCoF as:

$$\Delta P_{\text{i\_pu}} = -2H_v \cdot \frac{d}{dt}\Delta f_{\text{g\_pu}} \tag{3}$$

From (2) and (3), it can be obtained that:

$$\frac{d}{dt}\Delta f_{\text{g\_pu}} = \frac{1}{2(H_M + H_v)}\left(\Delta P_{\text{m\_pu}} - \Delta P_{\text{l\_pu}}\right) \tag{4}$$

Comparing (4) with (1), the system inertia is equivalently increased from H_M to $H_M + H_v$. To achieve this, the power converter of the wind turbine system should be proportionally linked with the grid RoCoF, as shown in (3). The corresponding controller design will be discussed in Section 3. Therefore, the essential point is to realize the dynamics of Equation (3) through proper control of the interfaced power converters, which will be detailed in Section 3.

3. Inertia Provision Control Strategy

As discussed previously, the control strategy of inertia provision can be mainly divided into two aspects. The first is the acquisition of the grid RoCoF value, whereas the second is to control the wind turbine system's active power variation according to Equation (3).

3.1. Acquistion of RoCoF

Conventionally, the grid RoCoF value is obtained by measuring the real-time grid frequency and calculating its derivation. Figure 6 is a schematic diagram of the conventional

approach for RoCoF value calculation [33,34]. Initially, the grid voltage waveform is obtained, and its frequency, f_g, can be detected through zero crossing or Fourier transformation. Then, a derivation block is implemented to calculate df_g/dt, i.e., RoCoF. However, directly differentiating the frequency signal would result in noise amplification and therefore a compromise the RoCoF calculation performance. To address this problem, a measuring window (defined as the number of frequency-measuring periods over which the RoCoF is calculated) is usually employed. However, there is a tradeoff between RoCoF measurement accuracy and noise-rejection capability. If the length of the measuring window is considerable, the noise due to the derivation can be well attenuated. However, the measured RoCoF value will be differ more from the real value. If the filtering capability of the measuring window is weak, the measured RoCoF would be closer to the real RoCoF, whereas noise cannot be attenuated well.

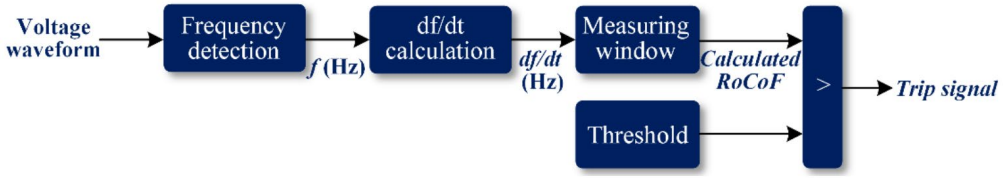

Figure 6. Conventional method for acquiring the grid RoCoF value.

To address this problem, a frequency-locked loop (FLL) is implemented in this paper for RoCoF calculation. In comparison with the conventional RoCoF calculation method, the FLL-based approach avoids the use of a derivation block and therefore provides noise-free RoCoF acquisition. Figure 6 displays the control block diagram of the FLL-based RoCoF acquisition, where v_g is the power grid voltage, $k_{\text{p-fll}}$ and $k_{\text{i-fll}}$ are the PI control parameters, and $v_{\text{fll-}\alpha}$ and $v_{\text{fll-}\beta}$ are the orthogonal signals obtained from a second-order generalized integrator (SOGI) [35,36].

From Figure 7, the frequency-domain transfer functions from v_g to $v_{\text{fll-}\alpha}$ and from v_g to $v_{\text{fll-}\beta}$ can be respectively derived as:

$$\frac{v_{\text{fll}-\alpha}(s)}{v_g(s)} = \frac{\omega_0 k_{\text{p}-\text{fll}} \cdot s}{s^2 + \omega_0 k_{\text{p}-\text{fll}} \cdot s + \omega_0^2} \tag{5}$$

$$\frac{v_{\text{fll}-\beta}(s)}{v_g(s)} = \frac{\omega_0^2 k_{\text{p}-\text{fll}}}{s^2 + \omega_0 k_{\text{p}-\text{fll}} \cdot s + \omega_0^2} \tag{6}$$

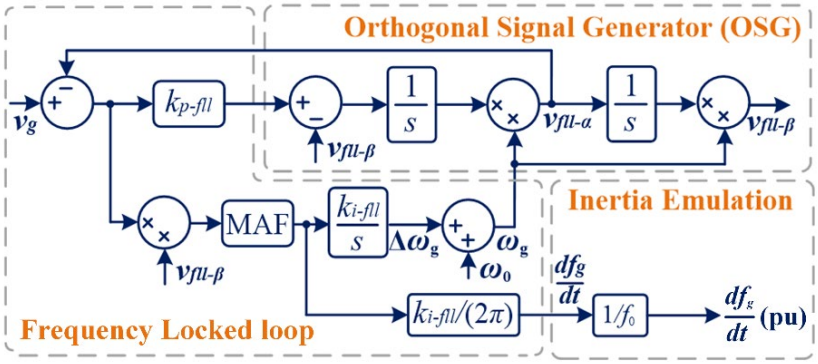

Figure 7. Control block diagram of the FLL-based RoCoF acquisition.

At the fundamental frequency, ω_0, it can be derived from (5) and (6) that:

$$|v_{\text{fll}-\alpha}(j\omega_0)| = |v_{\text{fll}-\beta}(j\omega_0)| = |v_g(j\omega_0)|, \tag{7}$$

$$\angle v_{\text{fll}-\alpha}(j\omega_0) = \angle v_g(j\omega_0) = \angle v_{\text{fll}-\beta}(j\omega_0) + \frac{\pi}{2}. \tag{8}$$

from which it is known that $v_{\text{fll-}\alpha}$ is in-phase with the grid voltage, v_g (with the same magnitude), whereas $v_{\text{fll-}\beta}$ is orthogonal with v_g (with the same magnitude). On this basis, the FLL dynamically adjusts $\Delta\omega_g$ through the integral controller, $k_{\text{i-fll}}/s$. By doing so, the frequency input of the SOGI, i.e., $\omega_0 + \Delta\omega_g$, can track with the real grid frequency. It should be noted that there is an inherent integral controller before $\omega_0 + \Delta\omega$. Therefore, the RoCoF can be obtained from the input of this integral controller, as illustrated in Figure 7. To further attenuate harmonic distortions and also improve the performance of RoCoF calculation, a moving average filter (MAF) is incorporated into the control loop, the time window of which should be properly selected to be one fundamental period, i.e., 20 ms for the 50 Hz power system.

In order to verify the efficacy of the RoCoF calculation, simulations were conducted, and the results are shown in Figure 8. In Figure 8, the RoCoF of the power grid voltage, v_g, changes from 0 Hz/s to −0.1 Hz/s at t = 0.5 s. It can be observed from Figure 8 that the obtained RoCoF value can quickly track with the real RoCoF value within around 100 ms.

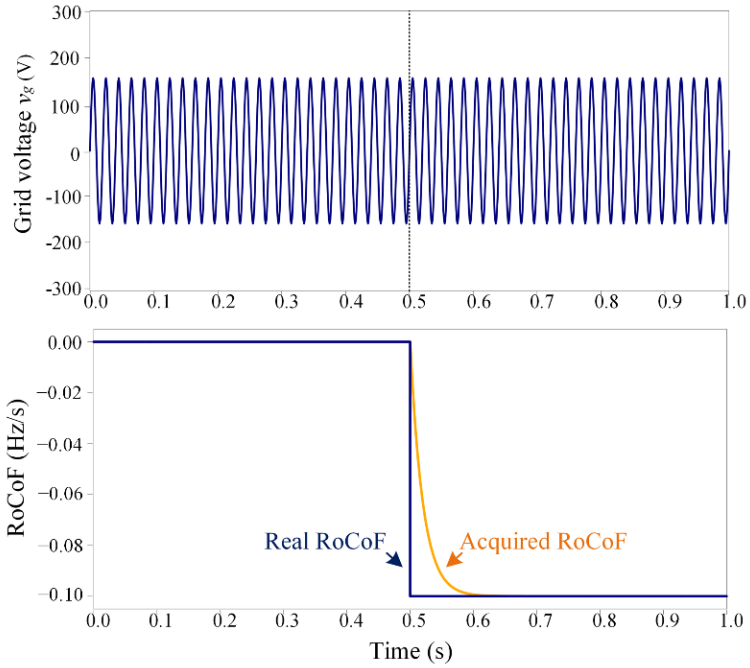

Figure 8. Simulation results for RoCoF acquisition.

3.2. DFIG System Control

Based on the acquired RoCoF value, the DFIG system can be controlled to provide the expected active power support (followed by inertia support). To achieve this target, the GSC is responsible for maintaining the DC-link voltage, v_{dc}, and regulating the reactive power, Q_g, injected to the grid. The RSC controls the induction machine.

3.2.1. GSC Control Scheme

Under the synchronous reference frame of the GSC, the relationship between the output voltage and output current is given by:

$$v_d = R_g i_d + L_g \frac{di_d}{dt} - \omega_0 L_g i_q + v_{\text{gd}} \tag{9}$$

$$v_q = R_g i_q + L_g \frac{di_q}{dt} + \omega_0 L_g i_d + v_{\text{gq}} \tag{10}$$

where v_d and v_q are the GSC output voltage and current, respectively; i_d and i_q are the GSC output and current, respectively; v_{gd} and v_{gq} are the grid voltages; and R_g and L_g are the grid resistance and inductance, respectively. The active and reactive power injected to the grid can be expressed as:

$$P_g = 3(v_d i_d + v_q i_q) \tag{11}$$

$$Q_g = 3(v_q i_d - v_d i_q) \tag{12}$$

A phase-locked loop (PLL) is usually implemented to obtain the phase angle information for the abc/dq transformation. The PLL dynamically regulates the phase angle such that $v_q = 0$. In this regard, the active power, P_g, is determined by the d-axis current, i_d, whereas the reactive power, Q_g, is determined by the q-axis current, i_q. On this basis, the current references for the GSC are given by:

$$i_{\text{dref}} = k_{\text{p1}}(v_{\text{dc}} - v_{\text{dc\_ref}}) + k_{\text{i1}} \int (v_{\text{dc}} - v_{\text{dc\_ref}})dt \tag{13}$$

$$i_{\text{qref}} = k_{\text{p2}}(Q_{\text{ref}} - Q_g) + k_{i2} \int (Q_{\text{ref}} - Q_g)dt \tag{14}$$

where $k_{\text{p1,2}}$ and $k_{\text{i1,2}}$ are the proportional and integral control gains, respectively; $v_{\text{dc\_ref}}$ is the reference DC-link voltage; and Q_{ref} is the reference reactive power. Figure 9 shows the control block diagram of the GSC, where the cross-coupling terms in Equations (8) and (9) have been decoupled through the current feedforward control, and k_{p3} and k_{i3} are the proportional and integral control gains, respectively, for the inner-loop current control.

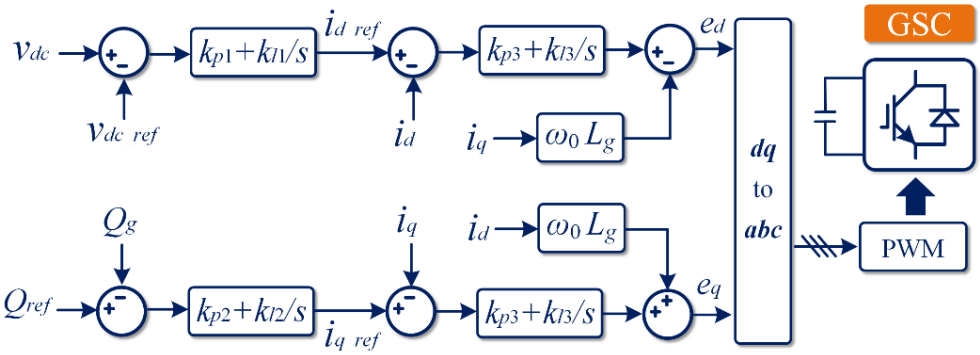

Figure 9. Control block diagram of the GSC.

3.2.2. RSC Control Scheme

Similarly, the dynamic equations of the induction machine can be expressed as:

$$\begin{cases} v_{\text{ds}} = R_s i_{\text{ds}} - \omega\lambda_{\text{qs}} + \frac{d}{dt}\lambda_{\text{ds}} \\ v_{\text{qs}} = R_s i_{\text{qs}} + \omega\lambda_{\text{ds}} + \frac{d}{dt}\lambda_{\text{qs}} \\ v_{\text{dr}} = R_r i_{\text{dr}} - (\omega - \omega_r)\lambda_{\text{qr}} + \frac{d}{dt}\lambda_{\text{dr}} \\ v_{\text{qr}} = R_r i_{\text{qr}} + (\omega - \omega_r)\lambda_{\text{dr}} + \frac{d}{dt}\lambda_{\text{qr}} \end{cases} \tag{15}$$

The stator and rotor flux linkages are given by:

$$\begin{cases} \lambda_{\text{ds}} = L_{\text{ls}} i_{\text{ds}} + L_m(i_{\text{ds}} + i_{\text{dr}}) \\ \lambda_{\text{qs}} = L_{\text{ls}} i_{\text{qs}} + L_m(i_{\text{qs}} + i_{\text{qr}}) \\ \lambda_{\text{dr}} = L_{\text{lr}} i_{\text{dr}} + L_m(i_{\text{ds}} + i_{\text{dr}}) \\ \lambda_{\text{qr}} = L_{\text{lr}} i_{\text{qr}} + L_m(i_{\text{qs}} + i_{\text{qr}}) \end{cases} \tag{16}$$

where v_{dr} and v_{qr} are the rotor voltage, v_{ds} and v_{qs} are the stator voltage, λ_{dr} and λ_{qr} are the rotor flux, λ_{ds} and λ_{qs} are the stator flux, ω_e is the angular frequency of the reference frame, ω_r is the angular frequency of the rotor, L_{lr} is the self-inductance, and L_m is the mutual inductance. Electromagnetic torque can be expressed as:

$$T_e = \frac{3PL_m}{2L_r}(i_{qs}\lambda_{dr} - i_{ds}\lambda_{qr}) = K_T(i_{qs}\lambda_{dr} - i_{ds}\lambda_{qr}) \quad (17)$$

By aligning the rotor flux vector with the d-axis of the synchronous reference frame, λ_{qr} equals zero. In this case, the electromagnetic torque is proportional to the q-axis stator current, i_{qs}, whereas the d-axis stator current is responsible for producing the flux. Figure 10 shows the control block diagram of the RSC, where the indirect field-oriented control is implemented for the rotor flux orientation [37] and T_{ref} is the reference electromagnetic torque.

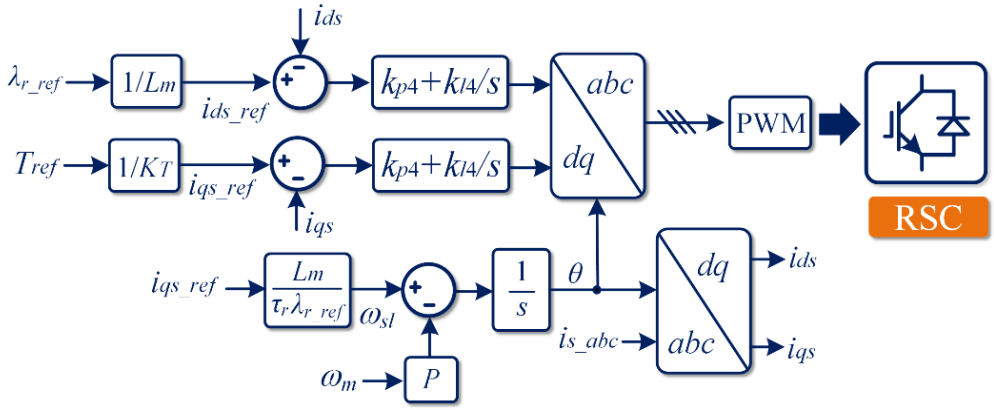

Figure 10. Control block diagram of the RSC.

The determination of the reference electromagnetic torque T_{ref} is displayed in Figure 11. It can be observed that the virtual inertia control, as well as the speed recovery control, are simultaneously incorporated into the control loop. ω_{r_ref} represents the desired rotor speed that achieves the maximum power harvest, P_{set} is the active power setpoint as determined by ω_{r_ref}, and H_v is the virtual inertia coefficient. It should be mentioned that the PI control gain, k_{p5} and k_{i5}, should be properly designed so that the virtual inertia control response time is much less than 10 s (the typical power system inertia response time). In addition, the PI control gain, k_{p6} and k_{i6}, need to be designed so that the speed recovery control response time is much more than 10 s. In this regard, the conflict between two control loops can be avoided. The objectives of inertia provision and speed recovery can be realized under a multi-timescale approach.

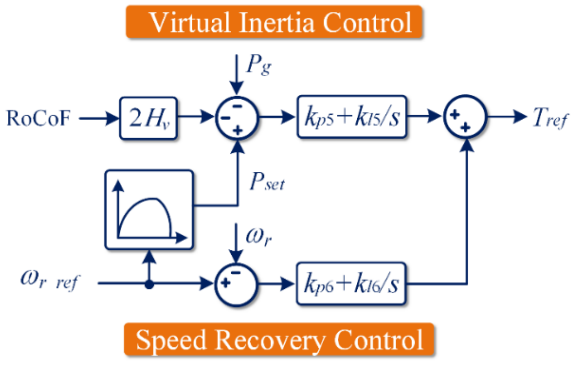

Figure 11. Control block diagrams for virtual inertia and speed recovery.

4. Simulation Results

To verify the theoretical analysis that the rotor speed recovery bandwidth will affect the inertia emulation effect and the effectiveness of the proposed multi-timescale controller, simulations were conducted in the PLECS (piece-wise linear simulation of electrical circuits) environment. The DFIG wind power generation system (schematic diagram shown in Figure 1) is connected to a practical power grid represented by an SM (primary frequency control framework illustrated in Figure 2). The power grid primary frequency regulation framework is illustrated in Figure 5. The main circuit and control parameters are listed in Table 1.

Table 1. Circuit and control parameters for the simulation.

Parameter	Description	Value
R	Frequency droop slope (p.u.)	0.05
T_G	Speed governor constant	0.1 s
F_{HP}	Turbine HP constant	0.3 s
T_{RH}	Reheater time constant	7.0 s
T_{CH}	Inlet volume time constant	0.2 s
D	Load-damping coefficient (p.u.)	1.0
H_M	Synchronous machine inertia (p.u.)	5.0 s
V_g	Grid voltage magnitude	1000 V
ω_0	Nominal grid frequency	100·π rad/s
VA_{base}	System base power (1 p.u.)	10 MW
J_r	Moment of inertia (turbine rotor)	75 kg·m^2
H_v	Virtual inertia (p.u.)	2.0 s
$\omega_{\mathrm{r\_ref}}$	Reference rotor speed	300 rad/s
P_{set}	Active power set power	2.5 MW

Figure 12 shows the simulation results when the DFIG generation system does not provide inertia support to the grid. At t = 5 s, a 5% step load change happens, and the power system frequency drops. As shown in Figure 12, the frequency nadir is 49.73 Hz, and the maximum RoCoF is −0.2 Hz/s. It can also be observed in Figure 12 that the wind turbine rotor speed, ω_r, is decoupled from the grid frequency, as well as the RoCoF value (i.e., there is almost no change in ω_r during the frequency event). This indicates that the mechanical energy stored in the rotor was not released to support the primary frequency response of the power system.

Figure 13 shows the simulation results when the DFIG system provides inertia support. The speed recovery control bandwidth is designed to be 0.03 Hz according to the multi-timescale control concept discussed in Section 3. Similarly, a 5% step load change happens when t = 5 s. It is observed that the wind turbine rotor speed is reduced during the inertia response period (5 s < t < 15 s). As a result, the rotor mechanical energy is released to support the grid frequency and limit the RoCoF. The frequency nadir is improved to 49.76 Hz, and the maximum RoCoF is reduced to −0.16 Hz/s. For a larger timescale (15 s < t < 40 s), the speed recovery control gradually takes effect, and the rotor speed comes back to the desired value of 300 rad/s. Note that the DC-link voltage is also under good control and remains close to the nominal value.

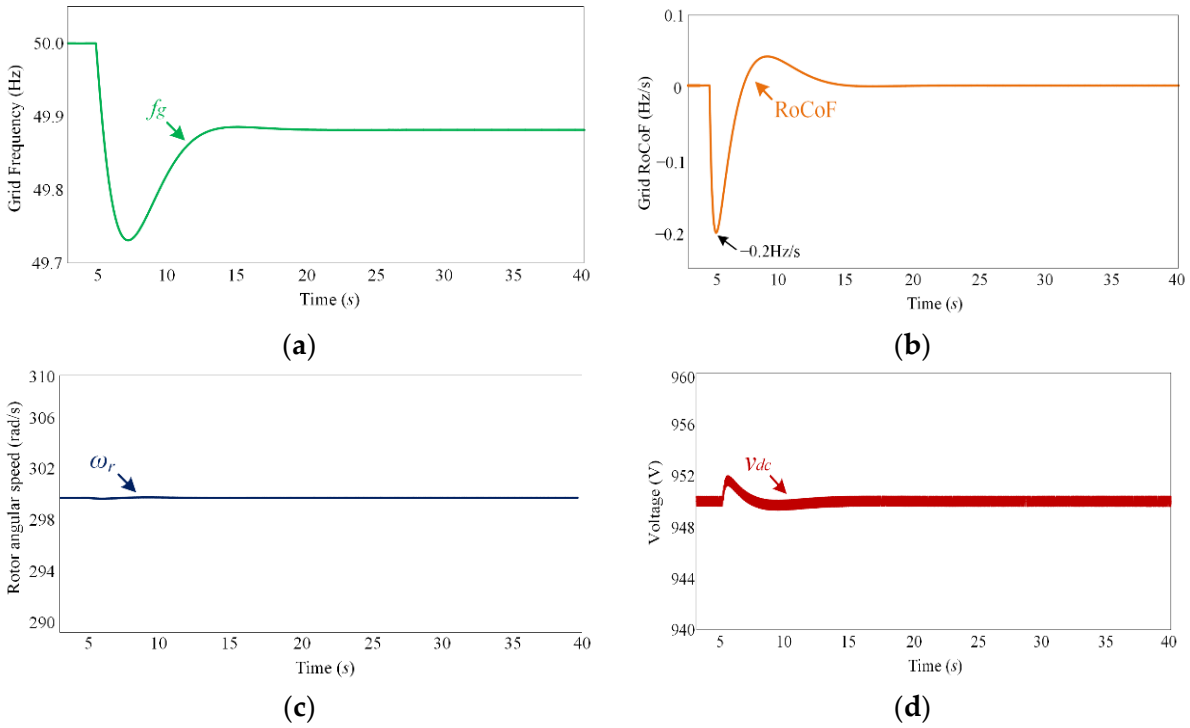

Figure 12. Simulation results when the DFIG system does not have an inertia-provision function. (**a**) Grid frequency; (**b**) grid RoCoF; (**c**) rotor angular speed; (**d**) DC-link voltage.

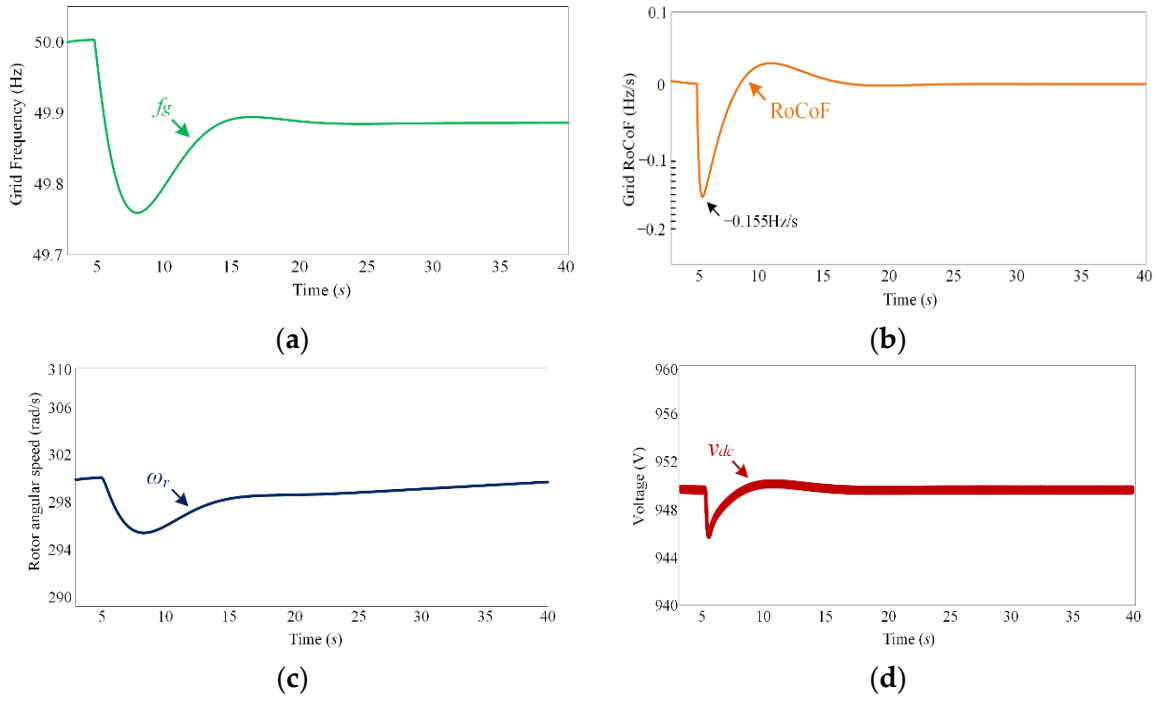

Figure 13. Simulation results when DFIG provides inertia support and the speed recovery control bandwidth is 0.03 Hz. (**a**) Grid frequency; (**b**) RoCoF; (**c**) rotor speed; (**d**) DC-link voltage.

For the next scenario, the speed recovery control bandwidth was intentionally adjusted to 0.1 Hz, which is close to that of the inertia response. Figure 14 displays the corresponding simulation results. Although the wind turbine rotor speed is decreased at the start of the frequency event, the coupling between the inertia control and the speed recovery control makes ω_r recover to the expected value within around 10 s. As a consequence, the inertia-

provision effect is compromised. The frequency nadir is 49.73 Hz, and the maximum RoCoF is −0.17 Hz/s, which is not as satisfactory as the results of the previous case.

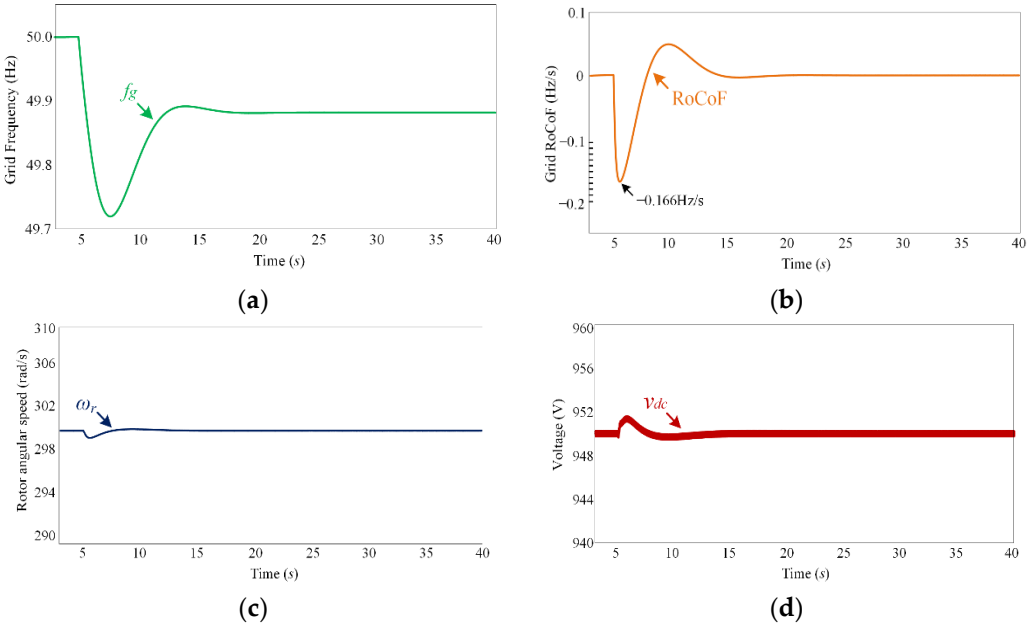

Figure 14. Simulation results when the DFIG system provides inertia support and the speed recovery control bandwidth is 0.1 Hz. (**a**) Grid frequency; (**b**) grid RoCoF; (**c**) rotor angular speed. (**d**) DC-link voltage.

Finally, the speed recovery control bandwidth was designed as 1 Hz, which is much faster than the inertia response. Figure 15 displays the simulation results. It is observed that the wind turbine rotor speed quickly recovers to 300 rad/s, even when it is subjected to the load change disturbance. Therefore, the mechanical energy of the turbine rotor does not effectively contribute to power grid frequency regulation. The scenario is similar to Figure 12, with a frequency nadir of 49.73 Hz and a maximum RoCoF of −0.2 Hz/s.

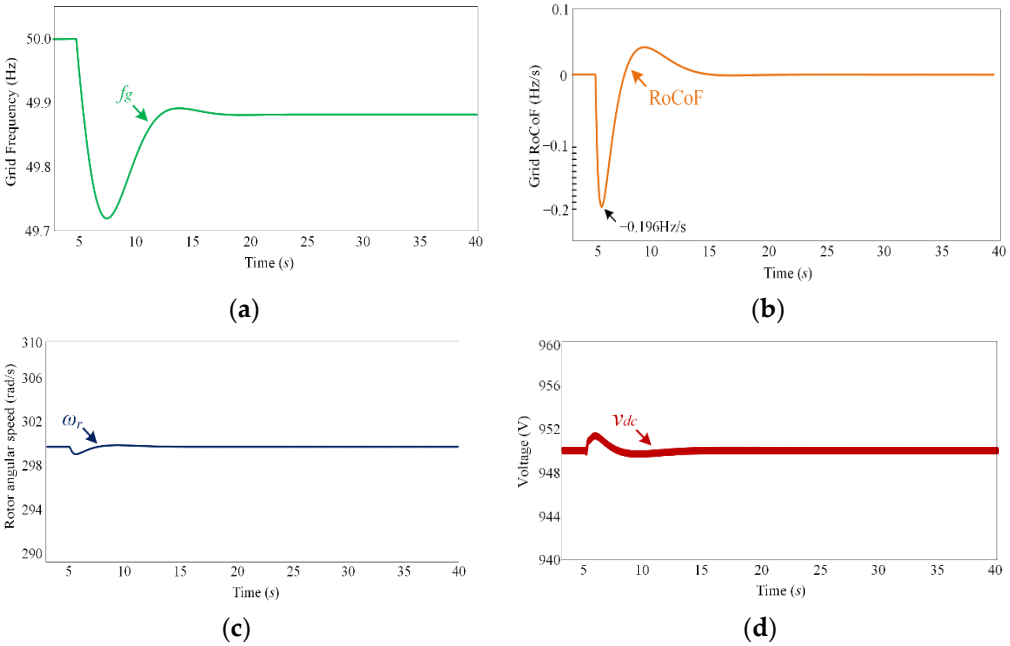

Figure 15. Simulation results when DFIG system provides inertia support and the speed recovery control bandwidth is 1 Hz. (**a**) Grid frequency; (**b**) RoCoF; (**c**) rotor speed; (**d**) DC-link voltage.

To summarize, Table 2 compares the simulation results. It is found that the maximum frequency error and maximum RoCoF for Case 2 are comparatively small. At the same time, the maximum rotor speed and DC-link voltage error for Case 2 are comparatively large. The DFIG for Case 2 satisfies the multi-timescale control principle proposed in this paper, whereas other cases do not. As a result, the mechanical energy stored in the rotor can be effectively released to support frequency regulation. This explains why the rotor speed error for Case 2 is larger and the frequency error/RoCoF are smaller.

Table 2. Error analysis for the simulation results.

Scenario	Maximum Frequency Error	Maximum RoCoF Error	Maximum Rotor Speed Error	Maximum DC-Link Voltage Error
Case 1 (Figure 12)	0.27 Hz	0.2 Hz/s	0.4 rad/s	1.9 V
Case 2 (Figure 13)	0.24 Hz	0.155 Hz/s	4.4 rad/s	5.3 V
Case 3 (Figure 14)	0.27 Hz	0.166 Hz/s	0.9 rad/s	1.7 V
Case 4 (Figure 15)	0.27 Hz	0.2 Hz/s	0.9 rad/s	1.7 V

5. Conclusions

In this paper, we analyzed the impacts of wind turbine speed recovery control on the inertia-provision effect. It was revealed through analysis that the emulated inertia is different from the physical inertia if the speed recovery control bandwidth is close to or higher than the inertia control bandwidth. On this basis, a multi-timescale control scheme was developed in this paper to decouple the speed recovery control and the inertia control so that the control conflict is avoided. Extensive simulations were conducted to verify the feasibility of the proposed method, and a 23% reduction in the power grid RoCoF and 11% reduction in the maximum frequency deviation were achieved through the proposed multi-timescale DFIG control.

Author Contributions: Conceptualization, Z.X. and Y.Q.; methodology, Y.Q.; software, Z.X.; validation, Z.X., Y.Q. and Y.Y.; formal analysis, Z.X.; investigation, Z.X. and Y.Q.; resources, W.L.; data curation, Z.X.; writing—original draft preparation, Z.X. and Y.Q.; writing—review and editing, W.L. and Y.Y.; visualization, Z.X.; supervision, Y.Q. and W.L.; project administration, Y.Q.; funding acquisition, Y.Y. All authors have read and agreed to the published version of the manuscript.

Funding: This project was supported by the National Natural Science Foundation of China (Project no.: 52107212).

Institutional Review Board Statement: Not applicable.

Informed Consent Statement: Not applicable.

Conflicts of Interest: The authors declare no conflict of interest.

References

1. Peng, Q.; Jiang, Q.; Yang, Y.; Liu, T.; Wang, H.; Blaabjerg, F. On the Stability of Power Electronics-Dominated Systems: Challenges and Potential Solutions. *IEEE Trans. Ind. Appl.* **2019**, *55*, 7657–7670. [CrossRef]
2. Fang, J.; Li, H.; Tang, Y.; Blaabjerg, F. On the Inertia of Future More-Electronics Power Systems. *IEEE J. Emerg. Sel. Top. Power Electron.* **2019**, *7*, 2130–2146. [CrossRef]
3. Microgrids, F.C.; Arco, S.D.; Suul, J.A. Equivalence of Virtual Synchronous Machines and Frequency-Droops for Converter-Based MicroGrids. *IEEE Trans. Smart Grid* **2014**, *5*, 394–395.
4. Huang, L.; Xin, H.; Wang, Z. Damping Low-Frequency Oscillations through VSC-HVdc Stations Operated as Virtual Synchronous Machines. *IEEE Trans. Power Electron.* **2019**, *34*, 5803–5818. [CrossRef]

5. Australian Energy Market Commission (AEMC), Mechanisms to Enhance Resilience in the Power System—Review of the South Australia Black System Event. *Tech. Rep.* **2019**. Available online: https://www.aemc.gov.au/sites/default/files/documents/aemc_-_sa_black_system_review_-_final_report.pdf (accessed on 11 February 2022).
6. Zhong, Q.C.; Weiss, G. Synchronverters: Inverters that mimic synchronous generators. *IEEE Trans. Ind. Electron.* **2011**, *58*, 1259–1267. [CrossRef]
7. Khajehoddin, S.A.; Karimi-Ghartemani, M.; Ebrahimi, M. Grid-supporting inverters with improved dynamics. *IEEE Trans. Ind. Electron.* **2019**, *66*, 3655–3667. [CrossRef]
8. Fang, J.; Li, H.; Tang, Y.; Blaabjerg, F. Distributed Power System Virtual Inertia Implemented by Grid-Connected Power Converters. *IEEE Trans. Power Electron.* **2018**, *33*, 8488–8499. [CrossRef]
9. Blaabjerg, F.; Teodorescu, R.; Liserre, M.; Timbus, A.V. Overview of control and grid synchronization for distributed power generation systems. *IEEE Trans. Ind. Electron.* **2006**, *53*, 1398–1409. [CrossRef]
10. Qi, Y.; Deng, H.; Liu, X.; Tang, Y. Synthetic Inertia Control of Grid-Connected Inverter Considering the Synchronization Dynamics. *IEEE Trans. Power Electron.* **2022**, *37*, 1411–1421. [CrossRef]
11. Zhang, R.; Fang, J.; Tang, Y. Inertia Emulation through Supercapacitor Energy Storage Systems. In Proceedings of the 2019 10th International Conference on Power Electronics and ECCE Asia (ICPE 2019-ECCE Asia), Busan, Korea, 27–30 May 2019; Volume 3, pp. 1365–1370. [CrossRef]
12. Yan, X.; Sun, X. Inertia and droop frequency control strategy of doubly-fed induction generator based on rotor kinetic energy and supercapacitor. *Energies* **2020**, *13*, 3697. [CrossRef]
13. Chen, T.; Guo, J.; Chaudhuri, B.; Hui, S.Y. Virtual Inertia from Smart Loads. *IEEE Trans. Smart Grid* **2020**, *11*, 4311–4320. [CrossRef]
14. Mutoh, N.; Ohno, M.; Inoue, T. A method for MPPT control while searching for parameters corresponding to weather conditions for PV generation systems. *IECON Proc. Ind. Electron. Conf.* **2004**, *3*, 3094–3099. [CrossRef]
15. Wang, X.; Yue, M.; Muljadi, E. PV generation enhancement with a virtual inertia emulator to provide inertial response to the grid. In Proceedings of the 2014 IEEE Energy Conversion Congress and Exposition (ECCE), Pittsburgh, PA, USA, 14–18 September 2014; pp. 17–23. [CrossRef]
16. Chen, Z.; Lasseter, R.H.; Jahns, T.M. Active power reserve control for grid-forming PV sources in microgrids using model-based maximum power point estimation. In Proceedings of the 2019 IEEE Energy Conversion Congress and Exposition (ECCE), Baltimore, MD, USA, 29 September–3 October 2019; pp. 41–48. [CrossRef]
17. Zhong, C.; Zhou, Y.; Yan, G. Power reserve control with real-time iterative estimation for PV system participation in frequency regulation. *Int. J. Electr. Power Energy Syst.* **2021**, *124*, 106367. [CrossRef]
18. Zhang, X.; Gao, Q.; Hu, Y.; Zhang, H.; Guo, Z. Active power reserve photovoltaic virtual synchronization control technology. *Chin. J. Electr. Eng.* **2020**, *6*, 1–6. [CrossRef]
19. Peng, Q.; Tang, Z.; Yang, Y.; Liu, T.; Blaabjerg, F. Event-Triggering Virtual Inertia Control of PV Systems with Power Reserve. *IEEE Trans. Ind. Appl.* **2021**, *57*, 4059–4070. [CrossRef]
20. Peng, Q. Coordination of Virtual Inertia Control and Frequency Damping in PV Systems for Optimal Frequency Support. *CPSS Trans. Power Electron. Appl.* **2020**, *5*, 305–316. [CrossRef]
21. Brisebois, J.; Aubut, N. Wind farm inertia emulation to fulfill Hydro-Québec's specific need. In Proceedings of the 2011 IEEE Power and Energy Society General Meeting, Detroit, MI, USA, 24–28 July 2011; Volume 7, pp. 1–7. [CrossRef]
22. Holdsworth, L.; Ekanayake, J.B.; Jenkins, N. Power system frequency response from fixed speed and doubly fed induction generator-based wind turbines. *Wind Energy* **2004**, *7*, 21–35. [CrossRef]
23. Ekanayake, J.; Jenkins, N. Comparison of the response of doubly fed and fixed-speed induction generator wind turbines to changes in network frequency. *IEEE Trans. Energy Convers.* **2004**, *19*, 800–802. [CrossRef]
24. Lalor, G.; Mullane, A.; O'Malley, M. Frequency control and wind turbine technologies. *IEEE Trans. Power Syst.* **2005**, *20*, 1905–1913. [CrossRef]
25. Guo, X.; Zhu, D.; Zou, X.; Jiang, B.; Yang, Y.; Kang, Y.; Peng, L. Dynamic Inertia Evaluation for type-3 Wind Turbines Based on Inertia Function. *IEEE J. Emerg. Sel. Top. Circuits Syst.* **2021**, *11*, 28–38. [CrossRef]
26. Van De Vyver, J.; De Kooning, J.D.M.; Meersman, B.; Vandevelde, L.; Vandoorn, T.L. Droop Control as an Alternative Inertial Response Strategy for the Synthetic Inertia on Wind Turbines. *IEEE Trans. Power Syst.* **2016**, *31*, 1129–1138. [CrossRef]
27. Li, Y.; Xu, Z.; Wong, K.P. Advanced Control Strategies of PMSG-Based Wind Turbines for System Inertia Support. *IEEE Trans. Power Syst.* **2017**, *32*, 3027–3037. [CrossRef]
28. Tian, X.; Wang, W.; Chi, Y.; Li, Y.; Liu, C. Virtual inertia optimisation control of DFIG and assessment of equivalent inertia time constant of power grid. *IET Renew. Power Gener.* **2018**, *12*, 1733–1740. [CrossRef]
29. Junyent-Ferré, A.; Pipelzadeh, Y.; Green, T.C. Blending HVDC-Link Energy Storage and Offshore Wind Turbine Inertia for Fast Frequency Response. *IEEE Trans. Sustain. Energy* **2015**, *6*, 1059–1066. [CrossRef]
30. Morren, J.; de Haan, S.W.H.; Kling, W.L.; Ferreira, J.A. Wind turbines emulating inertia and supporting primary frequency control. *IEEE Trans. Power Syst.* **2006**, *21*, 433–434. [CrossRef]
31. Xi, X.; Geng, H.; Yang, G. Small signal stability of weak power system integrated with inertia tuned large scale wind farm. In Proceedings of the 2014 IEEE Innovative Smart Grid Technologies-Asia (ISGT ASIA), Kuala Lumpur, Malaysia, 20–23 May 2014; pp. 514–518. [CrossRef]

32. Ma, J.; Qiu, Y.; Li, Y.; Zhang, W.; Song, Z.; Thorp, J.S. Research on the impact of DFIG virtual inertia control on power system small-signal stability considering the phase-locked loop. *IEEE Trans. Power Syst.* **2017**, *32*, 2094–2105. [CrossRef]
33. Ten, C.F.; Crossley, P.A. Evaluation of ROCOF relay performances on networks with distributed generation. In Proceedings of the 2008 IET 9th International Conference on Developments in Power System Protection (DPSP 2008), Glasgow, UK, 17–20 March 2008; pp. 522–527. [CrossRef]
34. DNV GL Energy Advisory (for EirGrid plc), RoCoF Alternative Solutions Technology Assessment: High level assessment of frequency measurement and FFR type technologies and the relation with the present status for the reliable detection of high RoCoF events in a adequate time frame. Tech. Rep., No. 16011111, rev. 005. 2015. Available online: https://www.eirgridgroup.com/site-files/library/EirGrid/RoCoF-Alternative-Solutions-Technology-Assessment-Phase-1-DNV-GL-Report_.pdf (accessed on 11 February 2022).
35. Qi, Y.; Yang, T.; Fang, J.; Tang, Y.; Potti, K.R.R.; Rajashekara, K. Grid Inertia Support Enabled by Smart Loads. *IEEE Trans. Power Electron.* **2021**, *36*, 947–957. [CrossRef]
36. Fang, J.; Zhang, R.; Li, H.; Tang, Y. Frequency Derivative-based Inertia Enhancement by Grid-Connected Power Converters with a Frequency-Locked-Loop. *IEEE Trans. Smart Grid* **2018**, *10*, 4918–4927. [CrossRef]
37. Wu, B.; Narimani, M. *High-Power Converters and AC Drives*; John Wiley & Sons: Hoboken, NJ, USA, 2017.